

A PHOTOMETRIC SYSTEM FOR DETECTION OF WATER AND METHANE ICES ON KUIPER BELT OBJECTS*,†

CHADWICK A. TRUJILLO¹, SCOTT S. SHEPPARD², AND EMILY L. SCHALLER³

¹ Gemini Observatory, Northern Operations Center, 670 N. A'ohoku Place, Hilo, HI 96720, USA; trujillo@gemini.edu

² Carnegie Institution of Washington, 5241 Broad Branch Rd. NW, Washington, DC 20015, USA; sheppard@dtm.ciw.edu

³ Lunar and Planetary Laboratory, 1629 E. University Blvd., Tucson, AZ 85721-0092, USA; els@lpl.arizona.edu

Received 2010 August 3; accepted 2011 January 24; published 2011 March 10

ABSTRACT

We present a new near-infrared photometric system for detection of water ice and methane ice in the solar system. The system consists of two medium-band filters in the *K*-band region of the near-infrared, which are sensitive to water ice and methane ice, plus continuum observations in the *J* band and *Y* band. The primary purpose of this system is to distinguish between three basic types of Kuiper Belt Objects (KBOs)—those rich in water ice, those rich in methane ice, and those with little absorbance. In this work, we present proof-of-concept observations of 51 KBOs using our filter system, 21 of which have never been observed in the near-infrared spectroscopically. We show that our custom photometric system is consistent with previous spectroscopic observations while reducing telescope observing time by a factor of ~ 3 . We use our filters to identify Haumea collisional family members, which are thought to be collisional remnants of a much larger body and are characterized by large fractions of water ice on their surfaces. We add 2009 YE₇ to the Haumea collisional family based on our water ice band observations ($J - H_2O = -1.03 \pm 0.27$) which indicate a high amount of water ice absorption, our calculated proper orbital elements, and the neutral optical colors we measured, $V - R = 0.38 \pm 0.04$, which are all consistent with the rest of the Haumea family. We identify several objects dynamically similar to Haumea as being distinct from the Haumea family as they do not have water ice on their surfaces. In addition, we find that only the largest KBOs have methane ice, and Haumea itself has significantly less water ice absorption than the smaller Haumea family members. We find no evidence for other families in the Kuiper Belt.

Key words: comets: general – Kuiper belt: general – Oort Cloud – planets and satellites: surfaces

1. INTRODUCTION

Detecting ices on small outer solar system bodies is of utmost importance because the presence of the most volatile ices, such as methane ice, may indicate primordial surfaces. The most massive of the known Kuiper Belt Objects (KBOs), such as Eris and Pluto, cannot retain surface ices for the age of the solar system even under moderate heating, temperatures of $\gtrsim 70$ K (Schaller & Brown 2007b). Thus, an inventory of volatile ices on the KBOs has the potential to provide a useful metric of historical heating. In the absence of planet-wide resurfacing, those KBOs that originally had ices but passed too close to the Sun would have lost them, and those which stayed distant could retain them. Tying the presence of surface ices to KBO orbital classes is one of the few direct observables which can shed light on the principal dynamical mechanisms involved in shaping the early Kuiper Belt.

Most ices of interest are bland or nearly so at visible wavelengths, but many show prominent absorption features at near-infrared wavelengths. Although many ices show strong features in the mid-infrared, at these wavelengths remote sensing via ground-based or space-based telescopes is severely hampered by thermal background radiation, making detection of ices dif-

ficult. Thus, nearly all surveys of KBOs to date that have positively identified ices have used near-infrared data to do so. The only major surface component which is not detectable in the near-infrared is the so-called ultra-red matter (Jewitt 2002), which appears in the visible and has not been definitively shown to be correlated with near-infrared colors.

Many researchers have collected near-infrared spectra of the brightest KBOs. Of the ~ 30 spectra of these bodies, almost all can be categorized into three types: water ice dominated, methane ice dominated, and neutral. For example, the five brightest KBOs (plus Pluto and Charon) can be divided into either water ice dominated (Charon, Haumea, Orcus, and Quaoar; Buie et al. 1987; Brown & Calvin 2000; Jewitt & Luu 2004; Trujillo et al. 2005, 2007a; Pinilla-Alonso et al. 2009; Fraser & Brown 2009) or methane ice dominated (Pluto, Makemake, Eris; Cruikshank et al. 1976; Brown et al. 2007a, 2005; Dumas et al. 2007; Merlin et al. 2009). Many of the fainter bodies have been shown to be featureless. There are some bodies that fall outside this broad taxonomy and have combinations of materials, such as Triton, which show significant absorption of combinations of substances (Quirico et al. 1999). Such bodies may not be adequately described by a simple set of photometric information. We note, however, that our survey goal is not to replace the detailed information that spectroscopy can yield, but to be able to identify population-wide trends and KBOs with unusual surfaces for follow-up spectroscopy. Although most bodies can be grossly characterized as either water or methane types, it is still important to note that many ices remain extremely difficult to detect in the near-infrared such as carbon monoxide (CO), carbon dioxide (CO₂), and nitrogen (N₂) due to the characteristically narrow and weak absorption lines of these ices and the extreme faintness of the KBOs. Even for Pluto,

* Based on observations obtained at the Gemini Observatory, which is operated by the Association of Universities for Research in Astronomy, Inc., under a cooperative agreement with the NSF on behalf of the Gemini partnership: the National Science Foundation (United States), the Science and Technology Facilities Council (United Kingdom), the National Research Council (Canada), CONICYT (Chile), the Australian Research Council (Australia), Ministério da Ciência e Tecnologia (Brazil), and Ministerio de Ciencia, Tecnología e Innovación Productiva (Argentina).

† This paper includes data gathered with the 6.5 m Magellan Telescopes located at Las Campanas Observatory, Chile.

which is over a factor of 10 brighter than the next brightest KBO, detection of CO, CO₂, and N₂ is challenging with modern instrumentation (Olkin et al. 2007). For this reason, tracing methane ice in the Kuiper Belt is extremely important as it is one of the few volatiles that is easily detectable and very sensitive to thermal history. Water ice acts as an important comparison ice, as it is not volatile beyond ~ 5 AU in the current solar environment, although like methane it can be destroyed by Galactic cosmic rays and solar UV photons, likely two of the dominant long-term weathering processes in the Kuiper Belt (Cooper et al. 2003).

There have been several photometric programs, with varying levels of success. Numerous attempts at *JHK* photometry have been published (see review work by Fulchignoni et al. 2008, and references therein), but unfortunately, these bandpasses are only serendipitously correlated with methane and water ice transitions and cannot readily discriminate between the two. Probably the most successful set of observations to date are those of Snodgrass et al. (2010), who surveyed Haumea family members in search of water ice in the *H* band. Their use of the medium bandpass *H_s* filter (1.52–1.63 μm), which probes the solid-state water ice region in KBOs, allowed the identification of many Haumea family members using their photometry and references to literature. Although the *H_s* filter is sensitive to water ice, it is much less sensitive to methane ice, which has peak absorption between 1.60 and 1.85 μm in the *H* band.

In this work, we introduce a simple custom-bandpass three-filter system which allows us to discern between KBOs with water ice, methane ice, and relatively bland surfaces. We have undertaken proof-of-concept observations which demonstrate that these filters are indeed consistent with spectroscopic observations yet typically require one-third of the telescope time of spectroscopic works. In addition, we have observed all of the Haumea family candidates brighter than $V = 22$ from Ragozzine & Brown (2007) and we identify which members have surfaces rich in water ice.

2. EXPERIMENTAL DESIGN

2.1. Custom Filter Bandpasses

Our filter set was chosen by simulating synthetic spectra of water ice, methane ice, and neutral KBO surfaces as observed through the Earth’s atmosphere using data from the Gemini/NIRI Integration Time Calculator to account for instrumental transmission and thermal emission. For the methane ice filter, regions in the *K* band were favored over the *H* band for four reasons: (1) the *H* band contains many more strong telluric OH emission lines than the *K* band, which are variable on ~ 5 minute timescales and may affect photometry, (2) transitions for methane and water in the *K* band are deeper than in the *H* band and are more widely separated from each other, (3) a wider bandpass without strong atmospheric extinction is available in the *K* band, and (4) the Gemini North telescope, used for the faintest bodies in this program, is optimized for near-infrared observations and thus has low emissivity and low thermal contamination in the *K* band. The possibility of double-bandpass “notch” filters including ice transitions in both the *H* band and the *K* band while excluding the sky between were also considered, but estimated signal gain was not sufficient to warrant the inclusion of the *H*-band telluric OH emission and the loss of throughput for the double-bandpass design.

In order to estimate the amount of absorption seen in the filter, continuum observations (i.e., observations out of absorption bands) are also needed as a reference point. Continuum

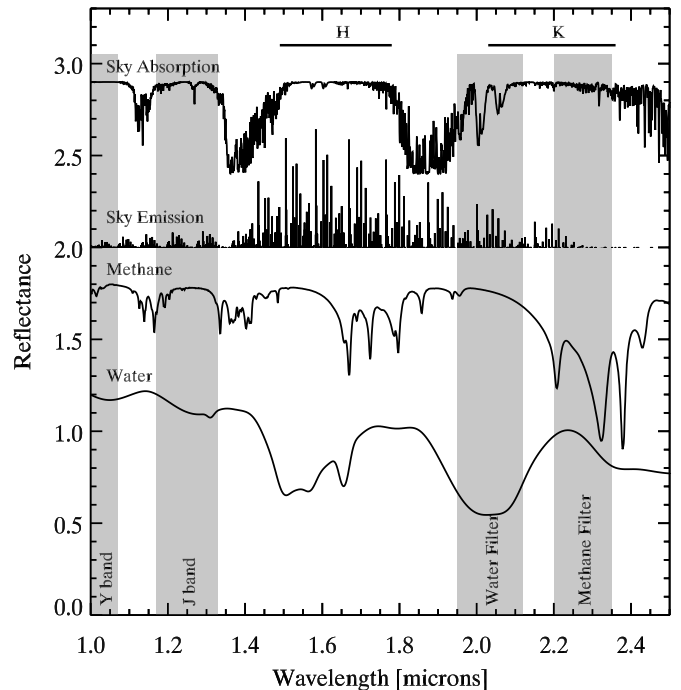


Figure 1. Our custom filter bands (gray regions) with synthetic water and methane ice spectra overlaid (bottom two traces, offset vertically for clarity). Our primary goal is the discrimination between water ice, methane ice, and featureless KBO surfaces. The top two traces show sky absorption and sky OH emission, the two main sources of systematic error in the near-infrared. The *Y* filter and *J* filter are used to sample the continuum by being as wide as possible while still minimizing ice and telluric effects. The “water” filter limits are set by telluric absorption on the blue end and the overlapping methane absorption on the red end. The “methane” filter limits are set by overlapping water absorption on the blue end and thermal emission on the red end. The methane filter also has some sensitivity to other alkanes which have C–H absorption in the methane region. The top portion of the plot shows traditional *HK* bandpasses, a poor diagnostic for ices.

observations must be in regions that have minimal (1) telluric absorption, (2) atmospheric emission, and (3) ice absorption from the target body. As seen in Figure 1, the optimum region that satisfies all three criteria is in the *J* band, where water, methane, and atmospheric contamination are minimal. There are no regions in either the *H* band or *K* band which are devoid of atmospheric, water, and methane ice absorption. We also collected *Y*-band data on many bodies as a mitigation against the presence of so called ultra-red material (Jewitt 2002), which can extend throughout the visible and contaminate the shortest wavelengths of the *J* band. After final analysis, robust results were obtained without the use of the *Y*-band filter data, but in a few cases, such as Quaoar, which is extremely red in the visible, it was needed (see Section 5.2.1). Final filter bandpasses are listed in Table 1.

2.2. Filter Manufacturing and Installation

We installed our filters into two telescopes—the 8.1 m mirror diameter Frederick C. Gillett Gemini telescope located atop Mauna Kea, Hawaii and the 6.5 m mirror diameter Magellan Baade Telescope, at Las Campanas, Chile. Our filters were manufactured by Barr Associates, Inc., in Massachusetts, USA, who implemented the bandpasses to our optical specifications. Filters with identical bandpasses were manufactured in the same coating batch to ensure consistent quality—only the geometric shape of the filter substrate differed between Gemini (60 mm diameter, round, 5 mm thick) and Magellan (32 mm across,

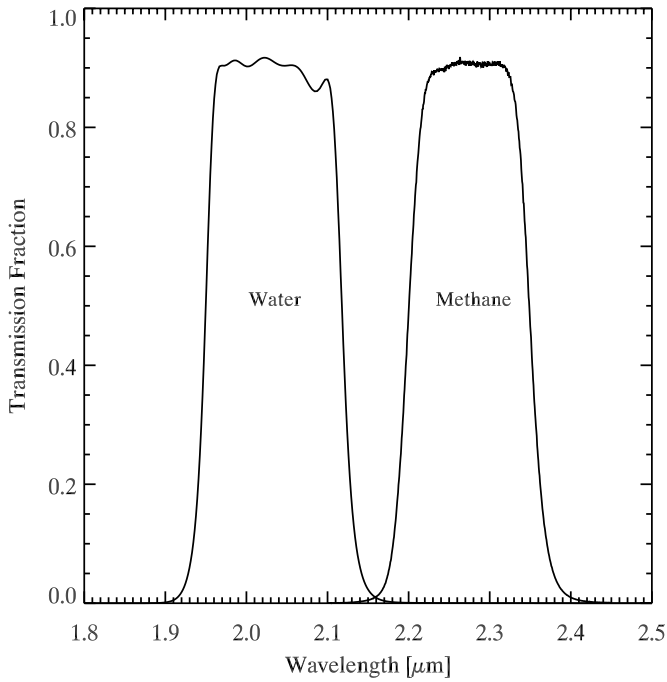


Figure 2. Efficiency curves for our two custom filters as a function of wavelength for the water ice filter (left) and the methane ice filter (right).

Table 1
Filter Wavelength Definitions

Filter	λ_{\min} (μm)	λ_{\max} (μm)	λ_{central} (μm)	$\Delta\lambda$ (μm)
Water	1.9490	2.1195	2.0343	0.1705
Methane	2.1990	2.3505	2.2748	0.1515

Notes. Wavelengths are defined to be the wavelength where the filter transmissions reached 50% of the maximum transmission. Minimum and maximum wavelengths are given by λ_{\min} and λ_{\max} , respectively, while central wavelength and filter widths are given by λ_{central} and $\Delta\lambda$, respectively.

square, 4 mm thick). The filter efficiencies are presented in Figure 2. Filters were installed in late 2008 in the Gemini North Near Infrared Imager and Spectrometer (NIRI; Hodapp et al. 2003) and in the Magellan Baade Persson’s Auxiliary Nasmyth Infrared Camera (PANIC; Martini et al. 2004) dewars. Both Gemini/NIRI and Magellan/PANIC are cryogenic instruments, so filter installations are performed very rarely, due to the minimum of two weeks warm up and cool down cycle time required to service the instruments. An extra set of Gemini/NIRI filters was manufactured to provide contingency in case unexpected manufacturing defects or installation problems were encountered.

2.3. Filter Commissioning and Transformation to Common Bandpasses

On-sky tests of the filters were performed shortly after installation to ensure acceptable quality of the filters. These tests involved imaging a UKIRT *JHK* standard star to estimate throughput and zero point and to ensure that image quality was consistent with other standard filters. A full characterization with additional targets has since been performed with a large number of UKIRT standards observed over several semesters at Gemini North. We present our custom color metrics versus standard color metrics in Equations (1) and (2), which are

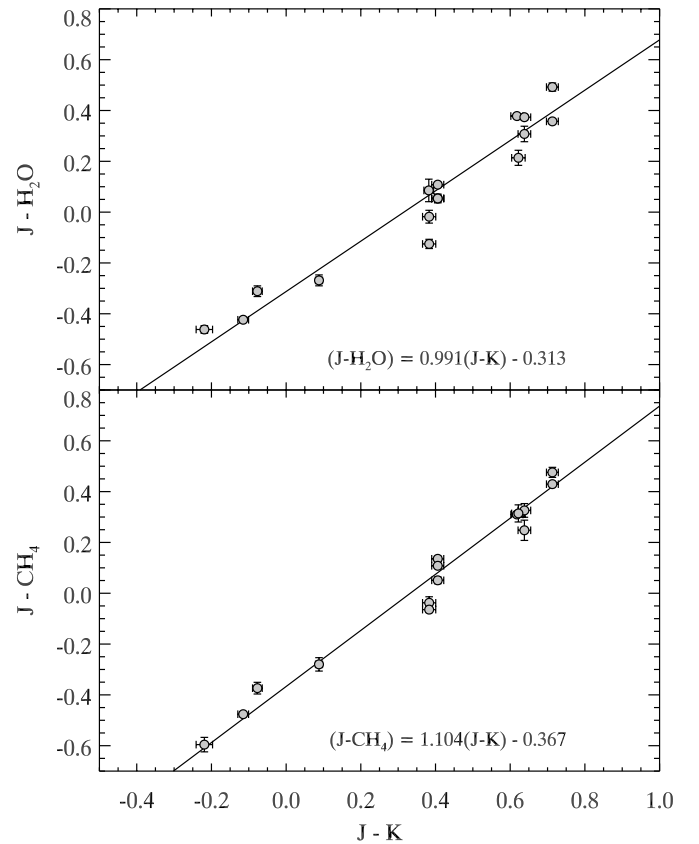


Figure 3. Photometric color calibration for Gemini/NIRI.

derived from the data displayed in Figure 3:

$$J - \text{H}_2\text{O} = 0.991(J - K) - 0.313, \quad (1)$$

$$J - \text{CH}_4 = 1.104(J - K) - 0.367. \quad (2)$$

It is important to note that while these transformations are applicable to UKIRT standard stars which generally have few transitions in the *K* band, they are not applicable to KBOs or other bodies with icy surfaces, as the entire purpose of our experiment is to probe the absorption regions of KBO ices.

Since the Gemini North NIRI instrument is also a spectrometer, spectra were collected of the filters at cryogenic temperatures indicating that the overall throughput was consistent with that measured in the Barr laboratory (Figure 2)—thus no degradation of filter performance occurred during installation or cooling to cryogenic temperatures. This was not possible to do with Magellan PANIC since it is an imager only; however, the Magellan filters were manufactured using the same techniques and in the same batch as the NIRI filters, so we expect that the filters are identical in their physical properties. Results of a few science targets observed with both instruments showed consistency.

3. NEAR-INFRARED OBSERVATIONAL PROGRAM

Near-infrared observations of the brightest targets were performed at Magellan on four nights spanning two observing runs on UT dates 2008 October 18–19 and 2009 April 3–4. Weather conditions were photometric for both runs with typical delivered image quality through our custom filters of 0.3–0.5 arcsec. Gemini observations were conducted in the Gemini North

Queue under program IDs GN-2008A-Q-4, GN-2008B-Q-40, GN-2009A-Q-6, and GN-2009B-Q-30. Observing conditions were set at 70 percentile or better for image quality (i.e., K -band image quality of 0.55 arcsec or better at zenith) and 50 percentile for cloud cover (i.e., photometric). This typically led to image quality similar to that seen at Magellan, from 0.3 to 0.5 arcsec delivered on the detector. A more complete summary of the objects and observational circumstances of the observations appears in Table 2.

At Magellan, the telescope was tracked at the sidereal rate, while at Gemini, the telescope was tracked at the non-sidereal rate of the object. These two methods were used for ease of execution at the telescope—at Magellan any non-sidereal tracking rates must be updated upon slew by hand, while at Gemini the telescope can automatically compute moving object position and tracking rates from orbital elements. Since we were limited to ~ 60 s exposures or shorter due to the thermal sky background, our objects, which typically have ~ 3 arcsec hr^{-1} apparent motion, moved less than one-fifth of a seeing disk during each image, resulting in image quality being identical for both the object and background stars no matter which guiding technique was employed.

While observing a science target, filters were cycled with repeated visits to the J band to allow for identification and correction of any light curve effects. A typical observational sequence for a faint target at Gemini was three images taken with 30 s exposure time (3×30 s) J , 6×60 s H_2O , and 6×60 s CH_4 repeated for 1.25 hr while offsetting the telescope between each exposure. In addition, a short sequence of 3×30 s Y was included in the beginning of the sequence as an additional constraint on any large scale color trends that might be visible in the $1 \mu\text{m}$ wavelength region.

Primary color calibration was done by observing a G2V solar analog star immediately before or after every science target at an air mass similar to the science observations. The aim of collecting these data was to estimate any telluric extinction or emission in the custom filter regions, which was particularly important in the H_2O filter which contains a known region of atmospheric attenuation, which could result in a $\sim 3\%$ photometric variation (~ 0.03 mag) if left uncorrected. These techniques are similar to what is routinely done for spectroscopic telluric correction to provide valid spectral information in the $2 \mu\text{m}$ wavelength region. This provides for the simplest possible measure of object reflectance—science target colors are compared to the G2V analog taken at similar air mass to immediately and directly calculate reflectance.

In addition to the G2V solar analog, a UKIRT standard star was observed every night science observations were conducted. This provided information about any possible long-term degradation of the filters which could affect our results if it occurred. No photometric change in filter sensitivity or color was observed over the course of our observations.

4. DATA REDUCTION

Basic data reduction was performed in a standard manner for near-infrared imaging and in a similar manner at both telescopes. First, daytime flat fields were examined to identify bad pixels (i.e., those pixels that did not respond linearly with a change of flat field level). These pixels were replaced with a median of nearby pixels on all science and calibration images. Flat fields at Gemini were constructed from daytime observations of a calibration source, while at Magellan sky frames were used. The science fields were divided by these flats to correct for the pixel-

to-pixel variations seen in the detector. At Magellan, the pixel-to-pixel variations were very minor as the detector was generally cosmetically pristine for a near-infrared array. Two deep images were then created for each target, consisting of all science frames taken of a particular object (1) digitally shifted to track the object at the non-sidereal rate of the object of interest and (2) digitally shifted to track at the sidereal rate to create a deep image of the star field. This allowed for the rejection of science observations where the science object encountered background stars during the course of the observations. Finally, synthetic aperture photometry was performed on all of the science and calibration targets.

Photometric calibration was performed on a nightly basis by identifying all calibration stars taken on a given night and plotting the stellar brightness as a function of air mass. Any deviant calibration targets were rejected as being stars misidentified as G2V in the Simbad Astronomical Database (Wenger et al. 2000), with spectral typing derived from the Michigan Catalogues of Two-Dimensional Spectral Types for HD stars (Houk & Cowley 1975). The remaining stars were used to create a telluric correction curve as a function of air mass. In general, these observations remained consistent on a nightly basis. These photometric calibrations were applied to the science observations to produce a relative reflectance measurement for each object.

5. RESULTS

The results of our work are presented in Figure 4. The basic goal of this work is to demonstrate that our custom filter bandpass can distinguish between the three basic types of bodies observed in the Kuiper Belt: water ice, methane ice, and neutral reflectance. This trend is readily apparent in Figure 4 as the vast majority of objects fall into the neutral category in the upper right. Most bodies with ice detection have water ice and occupy the left part of Figure 4. The two known bodies with methane ice, Makemake and Eris, are shown in the bottom right of the figure, clearly separated from all other objects.

In this proof-of-concept sample, we have studied the brightest KBOs for two reasons: (1) these bodies require less telescope time to study and (2) many of these bodies have spectroscopy already collected by other researchers which provides corroborative evidence that our survey is performing as expected. We believe that the current sample adequately demonstrates that our custom photometric filter system does indeed distinguish between these basic types of bodies as the three basic surface types are clearly discernible by eye. In future works, we will extend our survey to fainter bodies requiring more telescope time—bodies that to date have been inaccessible to spectroscopic studies. Even in our current sample, about 40% of our targets have no known spectra collected, primarily due to their faintness.

Table 3 provides verification data for this work. It lists the color quantities computed for each object and the surface type based on this color quantity. In addition, it also lists references to published works that provide spectroscopic verification of our basic surface identification. Discrepancies between the two methods occur only for bodies with low absorption, as discussed in Section 5.2. All of the bodies with strong water ice features show excellent correlation with published spectra. The identification of water ice among the Haumea family members, including the recently discovered object 2009 YE₇ (Robinowitz & Marsden 2010) as well as Ixion and Orcus, is discussed in Section 5.1. For the Haumea family, we find that the faintest

Table 2
Observational Circumstances

Object Number	Object Name	Provisional Designation	Site	UT Date	UT Time Range	Air Mass Range	J (s)	H ₂ O (s)	CH ₄ (s)	Calibration Sources
		2000 CN ₁₀₅	Gemini	2009 Feb 1	12:25–13:37	1.014–1.065	450	1440	1320	HIP24336, HIP55398
		2001 KD ₇₇	Gemini	2009 Jun 15	12:16–13:06	1.560–1.887	150	360	240	HIP90869
		2001 QC ₂₉₈	Gemini	2009 Aug 4	12:29–13:27	1.049–1.078	180	780	420	HIP111063, HIP117367, HIP9829
		2002 GH ₃₂	Gemini	2009 Jan 31	15:30–16:08	1.223–1.259	270	660	720	HIP23259, HIP49580, HIP49942
		2002 KW ₁₄	Gemini	2009 Jun 30	09:34–10:34	1.515–1.887	360	1080	1080	HIP78107, HIP80609
		2002 MS ₄	Magellan	2009 Apr 5	09:09–10:34	1.066–1.113	525	600	1170	HD110747, HD118928, HD138159 HD142801, HD170717, HD95868
		2002 XV ₉₃	Gemini	2009 Jan 31	10:05–10:43	1.455–1.715	270	660	720	HIP23259, HIP49580, HIP49942
		2003 FE ₁₂₈	Gemini	2009 Apr 15	12:33–13:13	1.241–1.336	270	720	600	HIP73606
		2003 UZ ₁₁₇	Gemini	2009 Sep 20	13:13–14:11	1.032–1.049	360	540	960	HIP19767, HIP7373
		2003 UZ ₁₁₇	Gemini	2009 Dec 30	06:11–07:07	1.035–1.071	360	960	1020	HIP117367, HIP18768, HIP19767
		2003 UZ ₄₁₃	Gemini	2009 Jan 9	07:18–08:01	1.105–1.205	270	660	960	HIP19767
		2004 NT ₃₃	Gemini	2009 Jun 24	12:55–13:50	1.004–1.025	360	1080	1080	HIP106356
		2004 NT ₃₃	Gemini	2009 Aug 6	10:39–11:36	1.012–1.074	330	960	1080	HIP106356
		2004 PT ₁₀₇	Gemini	2009 Sep 10	06:00–06:37	1.411–1.603	270	660	540	HIP111063, HIP117367
		2005 CB ₇₉	Gemini	2009 Jan 31	11:47–12:26	1.019–1.054	270	600	660	HIP23259, HIP49580, HIP49942
		2005 GE ₁₈₇	Gemini	2009 Jan 31	13:58–14:36	1.427–1.655	270	720	420	HIP23259, HIP49580, HIP49942
		2005 QU ₁₈₂	Gemini	2009 Sep 20	08:40–09:57	1.218–1.499	390	1440	1380	HIP19767, HIP7373
		2007 JH ₄₃	Magellan	2009 Apr 4	07:33–09:19	1.022–1.078	600	1320	1935	HD123385, HD138159, HD154805 HD77533, HD85538
		2008 LP ₁₇	Gemini	2009 Jun 29	07:39–08:51	1.183–1.361	450	1440	1380	HIP113050, HIP75923
		2009 YE ₇	Gemini	2009 Dec 30	07:20–07:59	1.146–1.154	270	480	660	HIP117367, HIP18768, HIP19767
		2009 YE ₇	Gemini	2010 Feb 21	05:42–06:35	1.231–1.405	330	720	420	HIP18768
(19308)		1996 TO ₆₆	Gemini	2009 Sep 18	09:56–10:45	1.011–1.048	270	660	660	HIP117367, HIP11747, HIP9829
(19308)		1996 TO ₆₆	Gemini	2009 Dec 30	05:23–06:03	1.058–1.132	270	600	540	HIP117367, HIP18768, HIP19767
(24835)		1995 SM ₅₅	Gemini	2009 Sep 18	13:13–14:07	1.007–1.044	270	1260	660	HIP117367, HIP11747, HIP9829
(26181)		1996 GQ ₂₁	Gemini	2009 Jun 30	07:49–09:01	1.193–1.395	450	1440	1260	HIP78107, HIP80609
(26375)		1999 DE ₉	Magellan	2009 Apr 5	02:09–04:07	1.140–1.223	450	1980	1665	HD110747, HD118928, HD138159 HD142801, HD170717, HD95868
(28978)	Ixion	2001 KX ₇₆	Gemini	2009 May 1	14:43–15:03	1.664–1.790	180	300	300	HIP83875, HIP84181
(38628)	Huya	2000 EB ₁₇₃	Magellan	2009 Apr 5	05:06–05:59	1.152–1.263	300	600	990	HD110747, HD118928, HD138159 HD142801, HD170717, HD95868
(40314)		1999 KR ₁₆	Gemini	2009 Jan 31	14:47–15:26	1.185–1.263	270	720	660	HIP23259, HIP49580, HIP49942
(47171)		1999 TC ₃₆	Magellan	2008 Oct 18	04:03–05:03	1.129–1.148	450	810	840	HD9729, HIP11747
(47932)		2000 GN ₁₇₁	Gemini	2009 May 16	10:44–11:24	1.384–1.550	270	720	660	HIP73606
(50000)	Quaoar	2002 LM ₆₀	Magellan	2009 Apr 5	07:23–07:54	1.111–1.181	300	300	300	HD110747, HD118928, HD138159 HD142801, HD170717, HD95868
(55565)		2002 AW ₁₉₇	Gemini	2009 Jan 31	12:40–13:18	1.146–1.261	270	660	720	HIP23259, HIP49580, HIP49942
(55565)		2002 AW ₁₉₇	Magellan	2009 Apr 4	02:06–02:57	1.229–1.312	450	660	660	HD123385, HD138159, HD154805 HD77533, HD85538
(55636)		2002 TX ₃₀₀	Gemini	2008 Nov 6	06:49–07:21	1.015–1.037	180	720	300	HIP394
(55636)		2002 TX ₃₀₀	Gemini	2009 Jan 10	04:35–04:53	1.041–1.065	360	300	300	HIP394
(55637)		2002 UX ₂₅	Magellan	2008 Oct 18	05:24–06:24	1.286–1.366	450	540	1080	HD9729, HIP11747
(55638)		2002 VE ₉₅	Gemini	2009 Feb 1	07:36–08:31	1.127–1.304	360	1080	1080	HIP24336, HIP55398
(65489)	Ceto	2003 FX ₁₂₈	Gemini	2009 May 13	08:00–08:52	1.061–1.129	240	780	660	HIP72855, HIP82233
(84522)		2002 TC ₃₀₂	Gemini	2009 Aug 4	13:55–14:36	1.028–1.086	270	720	720	HIP111063, HIP117367, HIP9829
(84922)		2003 VS ₂	Gemini	2008 Dec 2	10:49–11:27	1.081–1.147	270	720	720	HIP21333
(86177)		1999 RY ₂₁₅	Gemini	2009 Sep 19	11:08–12:23	1.225–1.595	420	1260	1260	HIP117367
(90377)	Sedna	2003 VB ₁₂	Gemini	2008 Dec 3	09:54–11:06	1.060–1.209	450	1440	1440	HIP18768
(90482)	Orcus	2004 DW	Magellan	2009 Apr 4	00:32–01:40	1.091–1.159	300	1080	1080	HD123385, HD138159, HD154805 HD77533, HD85538
(90568)		2004 GV ₉	Magellan	2009 Apr 4	06:10–07:15	1.001–1.032	900	300	480	HD123385, HD138159, HD154805 HD77533, HD85538
(119951)		2002 KX ₁₄	Gemini	2009 May 1	13:22–14:09	1.441–1.629	270	720	720	HIP83875, HIP84181
(120132)		2003 FY ₁₂₈	Magellan	2009 Apr 4	03:05–04:11	1.067–1.163	450	660	1260	HD123385, HD138159, HD154805 HD77533, HD85538
(120178)		2003 OP ₃₂	Magellan	2008 Oct 18	01:23–03:42	1.205–1.727	930	1200	2220	HD9729, HIP11747
(120347)		2004 SB ₆₀	Gemini	2008 Nov 28	04:53–06:08	1.006–1.085	450	1440	1440	HIP113688
(120348)		2004 TY ₃₆₄	Gemini	2009 Sep 18	12:00–12:40	1.167–1.196	270	720	720	HIP117367, HIP11747, HIP9829
(136108)	Haumea	2003 EL ₆₁	Magellan	2009 Apr 4	05:22–05:52	1.505–1.525	300	300	300	HD123385, HD138159, HD154805 HD77533, HD85538
(136108)	Haumea	2003 EL ₆₁	Magellan	2009 Apr 5	04:24–04:50	1.574–1.652	150	300	450	HD110747, HD118928, HD138159 HD142801, HD170717, HD95868
(136199)	Eris	2003 UB ₃₁₃	Magellan	2008 Oct 18	06:30–07:16	1.215–1.371	300	300	1020	HD9729, HIP11747

Table 2
(Continued)

Object Number	Object Name	Provisional Designation	Site	UT Date	UT Time Range	Air Mass Range	J (s)	H_2O (s)	CH_4 (s)	Calibration Sources
(136472)	Makemake	2005 FY ₉	Magellan	2009 Apr 4	04:34–05:05	1.881–1.891	150	300	510	HD123385, HD138159, HD154805 HD77533, HD85538
(145451)		2005 RM ₄₃	Magellan	2008 Oct 18	07:36–09:09	1.213–1.445	750	1260	1380	HD9729, HIP11747
(145451)		2005 RM ₄₃	Magellan	2008 Oct 19	08:43–09:32	1.359–1.584	300	810	1080	HIP18768
(145452)		2005 RN ₄₃	Gemini	2008 Nov 1	05:22–06:36	1.067–1.116	450	1440	1440	HIP110035, HIP394
(145453)		2005 RR ₄₃	Magellan	2008 Oct 19	04:15–05:58	1.203–1.498	600	1890	1260	HIP18768
(145480)		2005 TB ₁₉₀	Gemini	2009 Aug 7	09:34–10:48	1.119–1.338	420	1440	1380	HIP117367, HIP80609
(145480)		2005 TB ₁₉₀	Gemini	2009 Sep 10	07:12–08:26	1.132–1.371	450	1440	1440	HIP11063, HIP117367
(174567)		2003 MW ₁₂	Magellan	2009 Apr 5	06:17–07:16	1.235–1.451	450	660	990	HD110747, HD118928, HD138159 HD142801, HD170717, HD95868
(175113)		2004 PF ₁₁₅	Gemini	2009 Aug 8	10:56–12:12	1.378–1.407	450	1440	1440	HIP110512
(202421)		2005 UQ ₅₁₃	Gemini	2008 Nov 1	07:04–08:19	1.009–1.023	450	1440	1440	HIP110035, HIP394
(208996)		2003 AZ ₈₄	Gemini	2009 Jan 31	11:01–11:39	1.124–1.236	270	720	720	HIP23259, HIP49580, HIP49942
(208996)		2003 AZ ₈₄	Magellan	2009 Apr 5	00:23–01:53	1.359–1.630	600	1320	1440	HD110747, HD118928, HD138159 HD142801, HD170717, HD95868
(225088)		2007 OR ₁₀	Gemini	2009 Jun 29	12:38–13:50	1.213–1.321	450	1440	1380	HIP113050, HIP75923
(225088)		2007 OR ₁₀	Gemini	2009 Sep 16	08:10–09:25	1.212–1.239	450	1380	1440	HIP113050
(229762)		2007 UK ₁₂₆	Magellan	2008 Oct 19	06:23–08:23	1.113–1.184	360	2250	1380	HIP18768

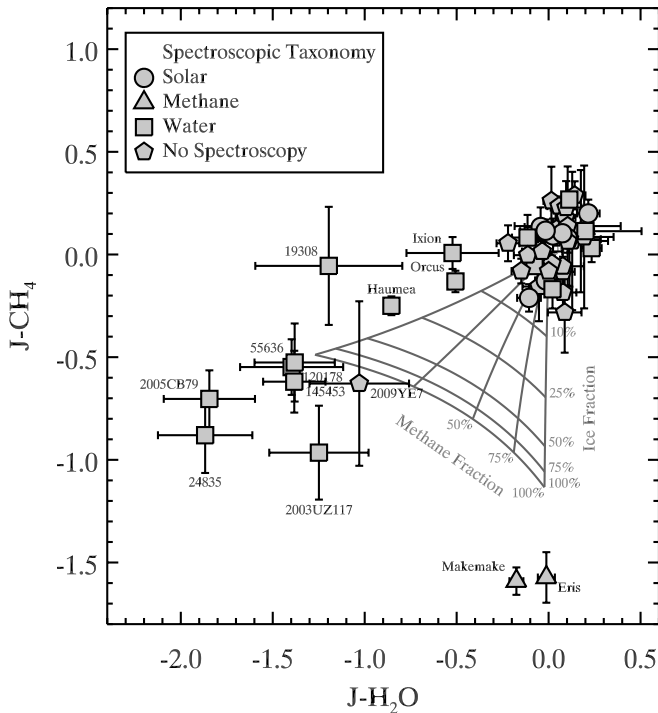


Figure 4. Combined photometry for all objects. Data symbol position is computed from our photometric survey. Data symbol shape is determined from published spectroscopy (see Table 3 for a complete list of references). Objects clearly fall into three groups: methane (Eris and Makemake), water (Haumea family members now including 2009 YE₇, Ixion, and Orcus), and neutral/low absorption (all others). In general, there is a strong correlation between our photometric work and published spectroscopic works for those bodies observed by both. The triangular gray grid represents colors expected for synthetic objects with varying percentages of methane, water, and total ice fraction. The vertical axis of the grid labeled as “ice fraction” represents total ice fraction (water and methane combined) with the remainder being represented by a neutral absorber. The diagonal axis labeled as “methane fraction” represents the total fraction of ice that is methane ice, with water ice being the remainder of the ice fraction. The model details are discussed in full in Section 5.2.

bodies systematically have the strongest transitions, as discussed in Section 6.1. In all cases, our photometric study was done in

far less time than spectroscopic identifications, as discussed in further detail in Section 6.2.

5.1. Family Members

5.1.1. Haumea Family

The Haumea family members are readily apparent by examining Figure 4 and cross-correlating icy bodies with orbital parameters. We present this cross-correlation in Table 4, where we list all bodies with $J - H_2O < -0.3$ (water ice bodies) or $J - CH_4 < -1.3$ (methane ice bodies). All of the Haumea family members are readily identifiable as having both water ice on their surfaces and having proper orbital elements, $i \sim 28^\circ$, $a \sim 43.5$ AU, and $e \sim 0.1$, as presented in Ragozzine & Brown (2007). We have observed all bodies brighter than $V = 22$ listed as possible Haumea family members on dynamical grounds from Ragozzine & Brown (2007) and report physical associations based on their high percentage of water ice, as summarized in Table 5. These identifications match previous spectroscopic works on the subject (Brown et al. 2007b; Schaller & Brown 2008; Snodgrass et al. 2010). We also report the identification of a possible new family member, 2009 YE₇, based on its unusually high water ice fraction and proper orbital elements which are similar to other Haumea members. We computed the proper orbital elements for 2009 YE₇ using an average of 20 million years of orbital motion computed by the MERCURY symplectic integrator (Chambers 1999).

5.1.2. 2009 YE₇

After determining that 2009 YE₇ was a Haumea family member, we proceeded to collect visible photometry of it to determine if it was consistent with the other Haumea family members which are neutral to slightly blue in reflectance, indicating not only that large amounts of water ice are on their surfaces, but that the water ice is in a largely pristine form.

Optical observations of 2009 YE₇ were obtained at The Magellan Clay 6.5 meter telescope on UT 2010 March 21. The LDSS3 camera has a STA0500A 4064 × 4064 Charge-Coupled Device with 15 μm pixels. The field of view is about 8.3 arcmin

Table 3
Photometry

Object Number	Object Name	Provisional Designation	J (mag)	$J - \text{H}_2\text{O}$ (mag)	$J - \text{CH}_4$ (mag)	Photometric Type	Spectroscopic Absorption ^a
		2000 CN ₁₀₅	20.48 ± 0.06	0.09 ± 0.09	-0.28 ± 0.20	Neutral	
		2002 KW ₁₄	19.69 ± 0.06	-0.05 ± 0.09	-0.16 ± 0.17	Neutral	
		2002 MS ₄	19.71 ± 0.27	0.18 ± 0.33	0.11 ± 0.30	Neutral	
		2002 XV ₉₃	19.80 ± 0.17	0.13 ± 0.19	0.07 ± 0.34	Neutral	
		2003 FE ₁₂₈	20.54 ± 0.13	0.19 ± 0.16	0.09 ± 0.35	Neutral	
		2003 UZ ₁₁₇	20.27 ± 0.07	-1.25 ± 0.27	-0.96 ± 0.23	Water ^b	~80% Water ²
		2003 UZ ₄₁₃	19.59 ± 0.07	0.08 ± 0.11	-0.06 ± 0.12	Neutral	
		2004 NT ₃₃	19.17 ± 0.04	-0.11 ± 0.08	0.00 ± 0.09	Neutral	
		2004 PT ₁₀₇	20.23 ± 0.11	0.11 ± 0.17	0.07 ± 0.23	Neutral	
		2005 CB ₇₉	19.61 ± 0.04	-1.84 ± 0.25	-0.70 ± 0.14	Water ^b	~70% Water ²
		2005 QU ₁₈₂	19.66 ± 0.28	0.10 ± 0.29	0.14 ± 0.29	Neutral	
		2007 JH ₄₃	19.36 ± 0.04	0.08 ± 0.07	-0.18 ± 0.10	Neutral	
		2008 LP ₁₇	19.74 ± 0.06	-0.03 ± 0.11	0.01 ± 0.10	Neutral	
		2009 YE ₇	20.84 ± 0.11	-1.03 ± 0.27	-0.63 ± 0.40	Water	
(19308)		1996 TO ₆₆	20.73 ± 0.23	-1.20 ± 0.40	-0.06 ± 0.29	Water ^b	Water ^{12,14}
(24835)		1995 SM ₅₅	19.43 ± 0.05	-1.87 ± 0.26	-0.88 ± 0.18	Water ^b	56% Water ¹
(26181)		1996 GQ ₂₁	19.12 ± 0.04	0.23 ± 0.05	0.03 ± 0.07	Neutral	9% Water ¹
(26375)		1999 DE ₉	19.25 ± 0.05	-0.02 ± 0.08	-0.05 ± 0.11	Neutral	Neutral ^{1,3}
(28978)	Ixion	2001 KX ₇₆	18.35 ± 0.07	-0.52 ± 0.25	0.01 ± 0.08	Water	~10% Water ^{3,13}
(38628)	Huya	2000 EB ₁₇₃	18.29 ± 0.03	0.06 ± 0.06	0.24 ± 0.05	Neutral	Neutral ^{1,11}
(40314)		1999 KR ₁₆	19.48 ± 0.03	0.01 ± 0.04	0.26 ± 0.17	Neutral	
(47171)		1999 TC ₃₆	18.00 ± 0.02	0.07 ± 0.03	0.10 ± 0.04	Neutral	8% Water ¹
(47932)		2000 GN ₁₇₁	19.07 ± 0.04	0.02 ± 0.09	0.09 ± 0.08	Neutral	Neutral ¹
(50000)	Quaoar	2002 LM ₆₀	17.25 ± 0.02	0.11 ± 0.03	0.27 ± 0.04	Neutral ^c	22% Water ^{4,6,10}
(55565)		2002 AW ₁₉₇	18.64 ± 0.04	0.09 ± 0.05	0.18 ± 0.06	Neutral	Neutral ^{1,3}
(55636)		2002 TX ₃₀₀	18.89 ± 0.05	-1.38 ± 0.22	-0.53 ± 0.19	Water ^b	64% Water ¹
(55637)		2002 UX ₂₅	18.48 ± 0.05	-0.02 ± 0.06	0.12 ± 0.05	Neutral	Neutral ¹
(55638)		2002 VE ₉₅	18.22 ± 0.02	-0.08 ± 0.03	-0.06 ± 0.03	Neutral	9% Water ¹
(65489)	Ceto	2003 FX ₁₂₈	19.61 ± 0.06	0.09 ± 0.08	0.23 ± 0.13	Neutral	14% Water ¹
(84522)		2002 TC ₃₀₂	18.93 ± 0.02	-0.02 ± 0.06	-0.13 ± 0.05	Neutral	Neutral ¹
(84922)		2003 VS ₂	18.19 ± 0.03	0.20 ± 0.05	0.11 ± 0.08	Neutral	7% Water ¹
(90377)	Sedna	2003 VB ₁₂	19.06 ± 0.04	0.02 ± 0.05	-0.17 ± 0.09	Neutral	~10% Water ⁷
(90482)	Orcus	2004 DW	18.12 ± 0.03	-0.51 ± 0.04	-0.13 ± 0.05	Water	~20% Water ⁹
(90568)		2004 GV ₉	18.55 ± 0.03	0.14 ± 0.06	0.29 ± 0.07	Neutral	
(119951)		2002 KX ₁₄	19.04 ± 0.07	-0.04 ± 0.09	0.13 ± 0.10	Neutral	Neutral ¹
(120132)		2003 FY ₁₂₈	19.09 ± 0.03	0.04 ± 0.09	0.12 ± 0.08	Neutral	Neutral ^{1,3}
(120178)		2003 OP ₃₂	19.37 ± 0.02	-1.40 ± 0.28	-0.55 ± 0.14	Water ^b	74% Water ¹
(120347)		2004 SB ₆₀	19.53 ± 0.05	0.22 ± 0.06	0.20 ± 0.07	Neutral	Neutral ²
(120348)		2004 TY ₃₆₄	18.75 ± 0.03	-0.11 ± 0.06	-0.21 ± 0.07	Neutral	Neutral ¹
(136108)	Haumea	2003 EL ₆₁	16.73 ± 0.03	-0.85 ± 0.04	-0.25 ± 0.05	Water ^b	~60% Water ⁴
(136199)	Eris	2003 UB ₃₁₃	17.99 ± 0.03	-0.01 ± 0.05	-1.57 ± 0.12	Methane	~95% Methane ⁸
(136472)	Makemake	2005 FY ₉	16.56 ± 0.02	-0.18 ± 0.04	-1.59 ± 0.07	Methane	~85% Methane ⁵
(145451)		2005 RM ₄₃	19.08 ± 0.02	-0.22 ± 0.06	0.05 ± 0.09	Neutral	
(145452)		2005 RN ₄₃	18.43 ± 0.02	0.11 ± 0.03	0.08 ± 0.03	Neutral	
(145453)		2005 RR ₄₃	19.20 ± 0.02	-1.38 ± 0.17	-0.62 ± 0.15	Water ^b	65% Water ¹
(145480)		2005 TB ₁₉₀	19.44 ± 0.04	0.00 ± 0.07	-0.08 ± 0.09	Neutral	
(174567)		2003 MW ₁₂	18.89 ± 0.02	0.08 ± 0.06	-0.08 ± 0.07	Neutral	
(175113)		2004 PF ₁₁₅	18.71 ± 0.02	0.02 ± 0.03	-0.04 ± 0.04	Neutral ^c	
(202421)		2005 UQ ₅₁₃	19.04 ± 0.04	0.10 ± 0.05	0.06 ± 0.06	Neutral ^c	
(208996)		2003 AZ ₈₄	19.37 ± 0.03	-0.11 ± 0.08	0.08 ± 0.11	Neutral	18%, ~ 25% Water ^{1,3}
(225088)		2007 OR ₁₀	19.06 ± 0.03	-0.15 ± 0.05	-0.08 ± 0.06	Neutral	

Notes. This table lists all objects observed and their surface types based upon our custom photometric system (this work). Spectroscopic surface types are based on other works as referenced in the table. Haumea family members are identified as being both water-ice-rich and having orbital parameters similar to Haumea.

^a Reported absorption refers to the percentage depth of the absorption feature, since surface fraction is a highly model-dependent quantity.

^b Likely Haumea family member based on composition (this work) and dynamics (Ragozzine & Brown 2007).

^c We find these three objects to be extremely red in the visible, indicating that a continuum measurement is difficult to obtain. These objects may have more absorption than indicated from the $J - \text{H}_2\text{O}$ or $J - \text{CH}_4$ metrics. We flag objects as “red” if they have $Y - J > 0.1$ to at least 3σ significance as determined from our photometry. See Section 5.2.1 for details.

References. (1) Barkume et al. 2008; (2) Schaller & Brown 2008; (3) Merlin et al. 2010; (4) Trujillo et al. 2007a; (5) Brown et al. 2007a; (6) Dalle Ore et al. 2009; (7) Trujillo et al. 2007b; (8) Brown et al. 2005; (9) Trujillo et al. 2005; (10) Jewitt & Luu 2004; (11) Jewitt & Luu 2001; (12) Brown et al. 2007b; (13) de Bergh et al. 2005; (14) Noll et al. 2000.

Table 4
Ice Detections from This Work

Object Number	Object Name	Provisional Designation	a^a (AU)	e^a	i^a (deg)	Dynamical Class
Haumea Family						
		2003 UZ ₁₁₇	44.26	0.13	27.88	Haumea
		2005 CB ₇₉	43.27	0.13	27.17	Haumea
(19308)		1996 TO ₆₆	43.32	0.12	28.02	Haumea
(24835)		1995 SM ₅₅	41.84	0.10	26.85	Haumea
(55636)		2002 TX ₃₀₀	43.29	0.13	26.98	Haumea
(120178)		2003 OP ₃₂	43.24	0.10	27.05	Haumea
(136108)	Haumea	2003 EL ₆₁	43.10	0.19	26.85	Haumea
(145453)		2005 RR ₄₃	43.27	0.13	27.07	Haumea
		2009 YE ₇	44.43	0.13	27.99	Haumea
Non-Haumea Water Ice						
(90482)	Orcus	2004 DW	39.17	0.23	20.56	3:2 Resonance
(28978)	Ixion	2001 KX ₇₆	39.62	0.25	19.65	3:2 Resonance
Methane Objects						
(136199)	Eris	2003 UB ₃₁₃	68.01	0.43	43.83	Scattered
(136472)	Makemake	2005 FY ₉	45.36	0.16	29.01	Classical

Notes. Bodies from our survey with significant amount of ices on their surfaces. The top section of the table are all Haumea family members based on their (1) water ice absorption and (2) the proximity of their proper orbital elements to Haumea as identified by Ragozzine & Brown (2007), with the exception of 2009 YE₇ which is identified in this work based on the proper orbital elements we computed, the water ice absorption depth, and the optical colors of the body. Orcus and Ixion are two non-family members with significant water ice absorption.

^a For the Haumea family members except for 2009 YE₇, a , e , and i are the proper orbital elements semimajor axis, eccentricity, and inclination, respectively, as presented by Ragozzine & Brown (2007). For 2009 YE₇, proper orbital elements are presented for the first time in this work, and are an average of 20 million years of orbital motion computed by the MERCURY symplectic integrator (Chambers 1999). The orbital elements for the non-Haumea family members are osculating elements provided by the Minor Planet Center.

Table 5
Near-infrared Observations of KBOs near the Haumea Family

Object Number	Object Name	Provisional Designation	$\Delta\nu_{\min}^a$ (m s ⁻¹)	T_p^a	Water Ice
(136108)	Haumea	2003 EL ₆₁	0	2.83	Yes
(19308)		1996 TO ₆₆	15.0	2.83	Yes
(145453)		2005 RR ₄₃	58.0	2.84	Yes
		2003 UZ ₁₁₇	60.8	2.84	Yes
		2005 CB ₇₉	66.5	2.84	Yes
(55636)		2002 TX ₃₀₀	68.4	2.84	Yes
(120178)		2003 OP ₃₂	91.4	2.85	Yes
		2009 YE ₇	~100	2.84	Yes
(24835)		1995 SM ₅₅	123.3	2.84	Yes
(202421)		2005 UQ ₅₁₃	39.0	2.84	No
(136472)	Makemake	2005 FY ₉	118.0	2.84	No
		2004 PT ₁₀₇	161.9	2.83	No
(120347)		2004 SB ₆₀	218.5	2.86	No
(40314)		1999 KR ₁₆	242.9	2.84	No

Notes. We list the bodies we observed that were also identified in Ragozzine & Brown (2007) as potential family members based on their dynamical association with Haumea, ordered by $\Delta\nu_{\min}$. The bodies with water ice detected appear to have lower $\Delta\nu_{\min}$ compared to those that have no water ice, although this result is not significant at the 3σ level.

^a As computed in Ragozzine & Brown (2007), excepting 2009 YE₇. The explicit computation of $\Delta\nu_{\min}$ for 2009 YE₇ is beyond the scope of this work. However, we include a crude estimate based on the fact that the proper orbital elements of 2009 YE₇ are close to those of 2003 UZ₁₁₇ and well within the $\Delta\nu = 150$ m s⁻¹ region of Figure 1 from Ragozzine & Brown (2007). We find in this work that 2009 YE₇ is a Haumea family member.

in diameter with a scale of 0.189 arcsec pixel⁻¹. Each image was reduced using dithered twilight flats and biases in a stan-

Table 6
Visible Photometry for 2009 YE₇ from This Work

Bandpass	Magnitude
r'	21.55 ± 0.03
$g' - r'$	0.45 ± 0.04
$r' - i'$	0.30 ± 0.05
R	21.35 ± 0.03 ^a
$B - R$	1.03 ± 0.04 ^a
$V - R$	0.38 ± 0.04 ^a
$R - I$	0.51 ± 0.05 ^a
$m_R(1, 1, 0^\circ)$	4.13 ± 0.05 ^a

Notes. At the time of the observations, 2009 YE₇ was at heliocentric distance 50.665 AU, geocentric distance 51.153 AU, and phase angle 0°:979. $m_R(1, 1, 0^\circ)$ refers to a hypothetical red magnitude at 1AU heliocentric and geocentric distance and phase angle of 0°.

^a Sloan colors were converted to the Johnson–Morgan–Cousins $BVRI$ color system using transfer equations from Smith et al. (2002), as described in Sheppard (2010).

dard manner. Images were acquired through Sloan g' , r' , and i' filters while the telescope was auto-guiding at sidereal rates using nearby bright stars. Exposure times were between 250 and 300 s. Southern Sloan standard stars were used to photometrically calibrate the data (Smith et al. 2005). In order to more directly compare our results with previous works, the Sloan colors were converted to the Johnson–Morgan–Cousins $BVRI$ color system using transfer equations from Smith et al. (2002), as in Sheppard (2010). These colors are presented in Table 6.

The optical colors of 2009 YE₇ have a spectral slope of $S(i' > g') = 5.3 \pm 3$, as defined in Doressoundiram et al. (2008) and implemented in Sheppard (2010). Such a spectral slope is consistent with the other Haumea family members, which have a weighted mean slope of $S = 1.9 \pm 0.3$, as computed from the values presented in Snodgrass et al. (2010). As the visible colors of 2009 YE₇ are inconsistent with most other KBOs, which have a mean $S \sim 20$ (Sheppard 2010), we consider the visible colors to be confirmation of the near-infrared photometric and dynamical identification of 2009 YE₇ as a Haumea family member.

5.1.3. Other Families

We find two objects in our survey have significantly more water ice on their surface than the other non-Haumea family members, namely Orcus and Ixion. These two bodies have low levels of water ice compared to the Haumea family members, as found by our survey and corroborated by spectroscopic studies which show possible detection of water ice (Trujillo et al. 2005; Barkume et al. 2008). These two bodies both occupy the 3:2 mean-motion resonance with Neptune and have inclinations within 1° of one another. Although a shared origin might be invoked for these bodies, adding in results of previous spectroscopic works suggests otherwise. Spectroscopic detections of water ice show no apparent correlation with inclination among the 3:2 resonance, as (47171), (55638), (84922), and (208996) have inclinations of 8.4° , 16.3° , 14.8° , and 13.6° , respectively (Table 3, and references therein). Thus, at the present time, we find no evidence for a family in the 3:2 resonance, although clearly there are bodies with moderate water ice present.

The 3:2 Neptune resonance is thought to have “swept” up many bodies shortly after the solar system formed due to Neptune’s outward migration (Malhotra 1993). Thus, even if there were a collisional family in the 3:2 resonance, there is likely to be many non-family members within the 3:2 resonance that have no water ice on their surfaces. Identifying a family among interlopers would be very difficult in the 3:2 resonance unless the collision happened very recently, of order ~ 100 kyr, over which time orbital elements can be stable for some objects. Much longer resonance habitation or large collisional velocities can cause profound departure (and ejection) of bodies, due to the very fine structure in the 3:2 resonance (Tiscareno & Malhotra 2009; Morbidelli et al. 2008).

It has been suggested that KBOs may be devoid or somewhat depleted of ices due to bombardment from solar UV photons and cosmic rays (Moroz et al. 2004; Cooper et al. 2003). These ionizing particles are expected to destroy the molecular bonds of simple ices, resulting in their depletion, and eventually yielding a dark, carbon-covered surface. Indeed, many faint KBOs have been studied spectroscopically, and in this work photometrically, the majority of which are neutral in reflectance. However, the presence of both methane ice and water ice, although the minority for all KBOs, is pervasive throughout the dynamical classes in the Kuiper Belt. In our survey, we find a Scattered KBO with ice (Eris), Resonant bodies (Ixion and Orcus), and Classical (Makemake) bodies with ices as shown in Table 4. Among previously published spectroscopic works, the same pervasive nature of water ice is apparent from Table 3 and references therein, with Scattered (Sedna and (26181)), Resonant ((47171), (55638), (84922), and (208996)), and Classical ((19308) and Quaoar) bodies. Thus, our survey and previous spectroscopic works independently suggest that ices are found among all orbital classes throughout the Kuiper

Belt and are thus not uniformly destroyed by solar UV photons and cosmic rays. Nor does it appear that ice surfaces are an extreme minority exception to the radiation processing scenario, as roughly 10% of the non-Haumea bodies in our survey have ice of some kind on their surfaces.

5.2. Sensitivity

Our sensitivity to ices can be estimated by comparing the results of our photometry with spectroscopic observations from literature, as seen in Table 3. For all of the Haumea family members, which exhibit extremely large water ice absorption from 55% to 80% depth in absorption, our photometric work and spectroscopic works agree. For non-Haumea bodies, some of which show very low levels of absorption ($\sim 15\%$ absorption depth), the results are somewhat discrepant, which marks the minimum absorption levels to which we are sensitive. In addition, bodies with significant quantities of ultra-red matter may have ices that are not easily detectable with our J -band continuum estimation.

5.2.1. Ultra-red Matter and J -band Continuum Estimation

A key quantity for estimating the amount of absorption in a spectrum is an accurate assessment of the continuum, i.e., the reflectance found outside of any absorption features. For our survey, we have chosen the J band because it is generally unaffected by ices, as described in Section 2.1. Unfortunately, the presence of the so-called ultra-red matter (Jewitt 2002) can still impact this estimate. The ultra-red matter, which primarily colors the visible, does extend partway into the J band to about $1.3 \mu\text{m}$. The best example of this spectroscopically is found for Quaoar (Jewitt & Luu 2004), which is one of the reddest KBOs in the visible (and thus has a large amount of ultra-red matter), but has a relatively colorless near-infrared continuum (attested by the fact that the near-infrared shape can be fit with a simple water ice model with no broad coloring agent). A careful examination of Quaoar’s spectrum indicates that the ultra-red matter likely extends into the J band, although the exact point where its absorption ends is not clear, since the spectral shape of the ultra-red matter is unknown. However, if we assume that Quaoar’s J -band spectrum differs from that of pure water ice only due to the contribution of ultra-red matter, then the maximum contamination that the ultra-red matter can impart to a J -band continuum measurement is 0.15 mag, which is significantly smaller than the ~ 1 mag of color difference between neutral and icy bodies in our experiment.

Thus, for Quaoar and any other bodies with extremely red visible slopes, the J -band continuum measurement could be depressed by 0.15 mag using our method. Thus, we use the $Y - J$ colors in our survey to identify extremely red KBOs, which could harbor more ices on their surfaces than our photometry indicates. We have flagged these bodies in Table 3 by examining the $Y - J$ colors we have collected. We indicate red bodies as being those bodies with $Y - J > 0.1$ to better than 3σ confidence. Of the 29 bodies with $Y - J$ known to better than 0.15 mag, only 3 bodies have such red colors: Quaoar, 2005 UQ₅₁₃, and 2004 PF₁₁₅. Thus, the point of rejecting objects with extreme $Y - J$ values is that red $Y - J$ color is a sign that the J -band flux measurement may be contaminated by ultra-red matter, and therefore ice detection may be depressed by not more than 0.15 mag.

5.2.2. Absorption Depth and Surface Ice Fraction

Rejecting the reddest objects in the sample yields a consistent picture between spectroscopy and photometry—our survey can identify objects with $\gtrsim 15\%$ water ice absorption depth. Ixion and Orcus were the two non-Haumea family members identified as having water ice by our photometric survey with band depths also measured by spectroscopy. They have $\sim 10\%$ and $\sim 20\%$ water ice absorption depths, respectively, as found by Trujillo et al. (2005), de Bergh et al. (2005), Barucci et al. (2008), and Merlin et al. (2010). Seven bodies were suspected to have water ice in spectroscopic works, but did not indicate water in our work, as shown in Table 3. The mean water ice band depth for these bodies is $12.5\% \pm 2.5\%$. Thus, we estimate that for our mean sample color accuracy of 0.1 mag, we are sensitive to water ice band depths $\gtrsim 15\%$. Since the bodies with large methane absorption show a similar ~ 1 mag separation from solar bodies in our system, we expect similar sensitivities for the methane band.

We also estimated our sensitivity by producing a very simple model of a range of bodies from neutral, to pure water ice, to pure methane ice, as shown in Figure 4. We use a simple bidirectional reflectance model similar to that described in Trujillo et al. (2005, 2007a), based on Hapke (1993). Using absorption coefficients for water ice Grundy & Schmitt (1998) and methane ice Grundy et al. (2002), we computed the full-disk albedo expected from a body covered in 1 mm diameter grains at 40 K. We computed a suite of models with these parameters, as presented as the gray triangular matrix in Figure 4. The vertical scale bar labeled as “ice fraction” represents total ice percentage (methane ice and water ice combined), with values less than 100% indicating the presence of a fictitious neutral absorber with albedo equal to the mean albedo of KBOs, 0.1 (Stansberry et al. 2008). The diagonal scale bar labeled as “methane fraction” indicates the percentage of methane ice, with values less than 100% including a linear combination of water ice. Thus, the top corner of the triangular grid represents a neutral body, the lower rightmost corner represents a body of 100% methane ice, and the leftmost corner represents a body of 100% water ice. Although many of the bodies in the graph appear to fall outside of the grid, this is expected for our crude three component model, as the real variety of surfaces on KBOs is certainly much more complex. The model does have utility, however, in that it provides a rough constraint on the minimum surface fraction of ice to which we are sensitive, roughly $\sim 10\%$ surface fraction in our model, which is consistent with the $\sim 15\%$ water band depth for both Orcus and Ixion.

6. DISCUSSION

6.1. Size versus Surface Type

We see two clear trends in our data set: (1) the surfaces of the smallest Haumea family members have a much stronger incidence of water ice than Haumea itself and (2) only the largest KBOs have methane ice.

6.1.1. Methane on Large Bodies

To date, there are only three bodies known in the Kuiper Belt with strong methane detections, Makemake and Eris, as shown by our survey in Figure 5 and Pluto. We use H as a proxy for size, which implicitly assumes a fixed albedo among the bodies, because the vast majority of bodies in the plot have unknown albedos. The possibility that only large bodies may

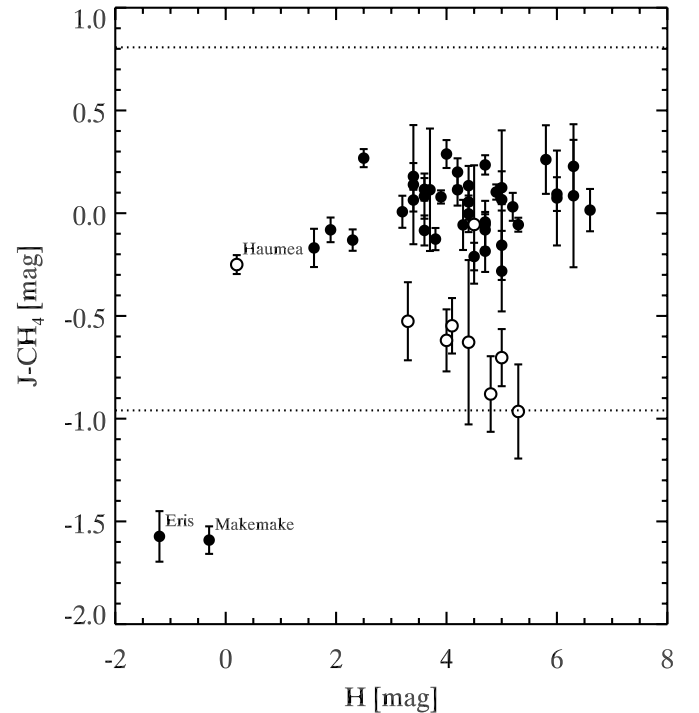


Figure 5. Methane ice as a function of size using the proxies $J - CH_4$ for methane ice fraction and H (absolute magnitude) as a proxy for size. Only the largest bodies in our sample, Makemake and Eris show evidence for methane ice. The dotted lines represent the $\pm 3\sigma$ limits to the non-methane bodies based upon their $J - CH_4$ values. Hollow circles are Haumea and its family members.

harbor methane ice was suggested by Schaller & Brown (2007b) and was used as the basis for a simple model explaining surface phenomena based on vapor pressure. Simply put, only very large bodies have surface gravity strong enough to overcome methane vapor pressure even at large heliocentric distances. We tested this theory measuring a large number of bodies with a variety of sizes with a single methodology. We find no strong evidence for methane on any bodies in our sample besides Makemake and Eris. Although both Quaoar and Sedna have been reported to have alkanes on their surfaces, neither has a large enough amount of the material to be detected in our survey (Jewitt & Luu 2004; Barucci et al. 2005; Schaller & Brown 2007a; Trujillo et al. 2007b; Emery et al. 2007). For our sample of 51 objects, the two with the smallest absolute magnitudes (a proxy for the largest size in the fixed albedo case) have methane ice. The probability that this could occur in size-neutral process which coated two of 51 bodies with methane ice is given by the binomial theorem as 0.12%, thus this possibility can be rejected with about 3.5σ confidence. To date, our observations are consistent with the Schaller & Brown (2007b) theory.

6.1.2. Water in the Haumea Family

Examining water ice on the Haumea family members, we find that water ice presence is inversely correlated with size, or the smallest bodies are the ones with the most water ice on their surface, as shown in Figure 6. In this figure, we use absolute magnitude, H , as a proxy for size since the albedos of Haumea’s progeny are unknown. Using H as a proxy for size implicitly assumes a fixed albedo among the bodies, which may not be the case. However, due to the large magnitude difference (~ 3 mag or a factor of 16 in flux) between Haumea and its progeny, it is extremely unlikely that even the brightest of the fainter bodies is larger than Haumea. We do not believe our

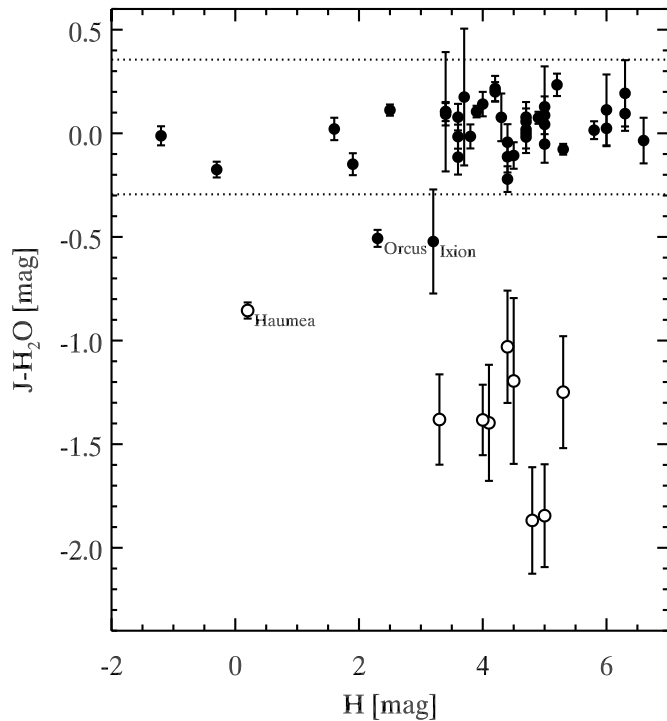


Figure 6. Water ice as a function of size using the proxies $J - H_2O$ for water ice fraction and H (absolute magnitude) as a proxy for size. The small Haumea family members show much larger water ice absorption than Haumea itself. This could be explained by (1) a larger surface fraction covered in water ice or (2) larger grain sizes. The dotted lines represent the $\pm 3\sigma$ limits to the non-family members based upon their $J - H_2O$ values. Orcus and Ixion fall outside of these 3σ limits and we thus consider them to have significant amounts of ice on their surfaces. Hollow circles are Haumea and its family members.

result to be due to any observational bias, as our standard star observations show no such correlation with apparent magnitude. We assess the statistical validity of this result by showing that the Haumea $J - H_2O = -0.85 \pm 0.04$ with $H = 0.2$ is significantly different from the rest of the Haumea family, all of which have $3.3 < H < 5.3$ and a population mean of $J - H_2O = -1.5 \pm 0.1$ (excluding 2009 YE₇). Thus, Haumea has less water absorption than the rest of the Haumea family with a confidence level of $\sim 6\sigma$.

It is not clear what is the underlying physical cause of such a difference; however, there are two obvious possibilities: (1) the smaller bodies have a larger fraction of water ice on their surfaces or (2) the smaller bodies have a larger grain size, leading to stronger absorption features. Both of these possibilities are physically plausible. If we assume that the Haumea family was created in a collisional event involving a much larger KBO, it is very likely that this body had some form of differentiation (McKinnon et al. 2008). Thus, the largest remaining member, Haumea, likely contains a larger fraction of rock in its core than the smaller family members which were created from the ejecta material, which was presumably closer to the surface, less dense, and with less structural strength than the Haumea material. Thus, it is easily plausible that scenario (1) is valid because the family members contain more water ice on a bulk level. Scenario (2) is also plausible since any ice transport is likely very strongly correlated with surface gravity. If significant surface evolution has taken place on the Haumea family, which has been suggested as a possible explanation for the crystalline water ice presence on their surfaces (Newman et al. 2008), then it is very likely that this process is affected by surface gravity. Surface

gravity profoundly affects ice transport and geologic processes such as cryovolcanism, thus nearly any evolutionary process whether is external (e.g., micro-meteorite bombardment leading to ice transport; Porter et al. 2010) or internal (e.g., cryovolcanism; Jewitt & Luu 2004) in origin likely is affected by body size. It should be noted that although cryovolcanism may be expected for larger bodies, in situ observations of the ~ 2700 km diameter Triton by *Voyager* show only a small amount of surface is likely affected by cryovolcanism (Abelson 1989). Theoretical modeling shows that cryovolcanism in large ($\gtrsim 1200$ km diameter) KBOs may be enhanced over that of Triton (Desch et al. 2009), making the role of cryovolcanism in disk-integrated surface properties still an open question.

6.2. The Role of Photometry in Future Work

Our custom photometric survey is not meant to replace spectroscopy in any way. The limited spectral information provided in a photometric survey covering only a few filters does not provide anywhere near the amount of information needed to disentangle the astrophysical processes taking place on minor bodies in the outer solar system. Indeed, in situ observations of Saturnian satellites such as Iapetus, Phoebe, and Hyperion show how remarkably diverse small body surfaces are in the outer solar system with extremely high signal-to-noise measurements. Thus, our survey is not meant to be an ending point of Kuiper Belt surface study but a starting point that will identify the bodies of greatest interest for later follow-up work.

Photometry does offer several distinct advantages over spectroscopy.

1. Numerous instrumental losses are associated with spectroscopy. Although each instrumental setup is different, observations from the Gemini North telescope are fairly typical for near-infrared instruments. Losses associated with an hour of NIRI spectroscopy would typically include the following: 20% loss from light near the periphery of the object that is occulted by the slit, 10% acquisition overhead required to put the target in the slit, and a 50% loss due to grism throughput and image quality degradation through the grism. In addition, spectral information is spread across a few thousand pixels of the detector, whereas photometric information is tightly associated in 20 pixels, greatly reducing instrumental noise.
2. Sky line removal can be difficult for spectral integrations which often require ~ 5 minute exposures for faint object signals to be apparent. Since OH lines emission can typically change on ~ 5 minute timescales, integrations longer than this can make sky line removal challenging. Since photometric integrations are typically of order ~ 1 minute, pairwise subtraction of images efficiently removes most of the changing sky background.
3. In crowded fields, potential contamination of bodies can be easily identified, as depicted in Figure 7. Spectroscopic observations typically only spend ~ 10 minutes imaging the science target during acquisition, with spectroscopic observations taking the vast majority of the telescope time. Thus, it is impossible to construct a deep-field image of the science target environment when performing spectroscopy, which, especially for objects near the galactic plane, can contain many contaminant background stars.

Because of these advantages, we find that we can save roughly a factor of ~ 3 in telescope time while still identifying the objects of key interest, such as the Haumea family members. This

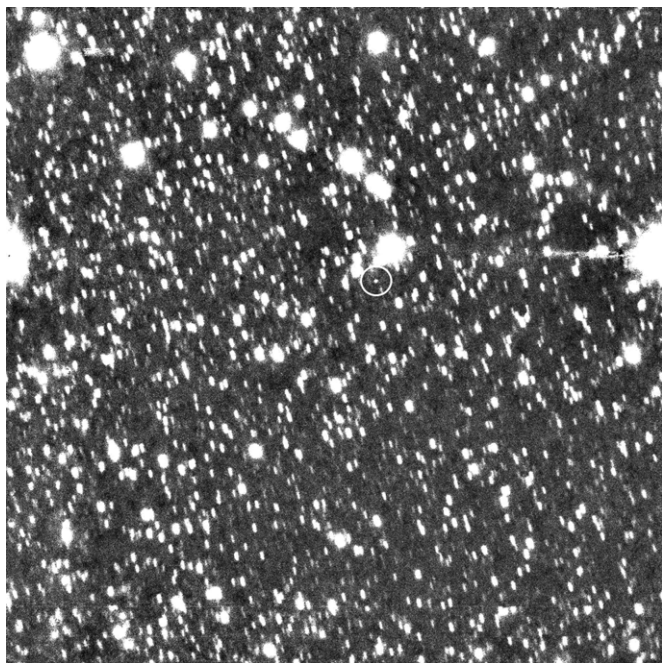


Figure 7. Example of a rich field from Magellan. The KBO 2002 MS₄ is shown in a deep composite image of all frames taken over a ~ 2 hr period, digitally tracked at the non-sidereal rate of the object. A deep image was constructed of every science field in our sample to ensure no stellar contamination. Such a verification procedure is not possible for traditional spectroscopic measurements and background stars can easily unknowingly contaminate observations.

gives us a large potential increase in sample size and allows us to observe many more objects with a consistent instrumental setup in consistent conditions than an equivalent spectroscopic work. In addition, a population-wide study such as ours has the ability to identify important population outliers for further spectroscopic study by the sheer number of objects available in our sample.

In this work, our primary goal is to present the details of the custom photometric filter system. A future work will include a much larger sample of bodies, including faint bodies that have to date been out of reach of spectroscopic works. Any bodies with unusual surface features will be identified for further study in a subsequent work. Since many of these bodies will be fainter than the $V \sim 22$ brightness level, they will require 10–30 hr of 10 m telescope time for follow-up spectroscopy to determine more about their surfaces. Requesting this amount of telescope time for a single object with no prior information about its surface is simply not feasible. Nor is it a wise use of telescope resources when most faint bodies appear to be bland. Thus, we believe that future results from our survey will become the cornerstone of spectroscopic study of faint bodies in the upcoming decade and as 30 m class telescopes begin to come on line.

7. SUMMARY

The primary purpose of this work is to detail our custom photometric system and demonstrate that it is useful in identifying dynamical correlations on the subset of KBOs we have observed to date. We find the following in this work.

1. Our custom photometric work can identify KBO surfaces with a factor of ~ 3 less telescope time than similar quality spectroscopic works. We can discriminate neutral bodies from water and methane ice bodies with $\gtrsim 15\%$ absorption

depths, which corresponds to approximately $\gtrsim 10\%$ surface fractions of ices for simple models of KBO surfaces.

2. We identify nine Haumea family members including a new object 2009 YE₇, which is consistent in visible color, water ice depth, and proper orbital elements with the rest of the Haumea family. We reject several objects with dynamics similar to Haumea because they do not have water ice on their surfaces.
3. We find that the smallest Haumea family members systematically have deeper water ice absorption than Haumea to 6σ confidence. This observation is consistent with a collisional origin for the system.
4. We identify two non-Haumea bodies with water ice in 3:2 mean-motion resonance with Neptune (Orcus and Ixion). Combining this with previous spectroscopic studies demonstrates that moderate water ice is pervasive throughout all Kuiper Belt dynamical classes.
5. Outside the Haumea family, we find no evidence for any correlation between body size and water ice fraction.
6. We find that only the largest KBOs harbor methane ice, which is consistent with arguments of volatile loss timescales based on surface gravity, such as those presented by Schaller & Brown (2007b).

We thank the anonymous reviewer for providing constructive comments which improved this work. Gemini observations were conducted under program IDs GN-2008A-Q-4, GN-2008B-Q-40, GN-2009A-Q-6, and GN-2009B-Q-30. This work was supported in part by NASA Planetary Astronomy Grant NNX07AK96G.

REFERENCES

- Abelson, P. H. 1989, *Science*, **246**, 1369
- Barkume, K. M., Brown, M. E., & Schaller, E. L. 2008, *AJ*, **135**, 55
- Barucci, M. A., Cruikshank, D. P., Dotto, E., Merlin, F., Poulet, F., Dalle Ore, C., Fornasier, S., & de Bergh, C. 2005, *A&A*, **439**, L1
- Barucci, M. A., et al. 2008, *A&A*, **479**, L13
- Brown, M. E., Barkume, K. M., Blake, G. A., Schaller, E. L., Rabinowitz, D. L., Roe, H. G., & Trujillo, C. A. 2007a, *AJ*, **133**, 284
- Brown, M. E., Barkume, K. M., Ragozzine, D., & Schaller, E. L. 2007b, *Nature*, **446**, 294
- Brown, M. E., & Calvin, W. M. 2000, *Science*, **287**, 107
- Brown, M. E., Trujillo, C. A., & Rabinowitz, D. L. 2005, *ApJ*, **635**, L97
- Buie, M. W., Cruikshank, D. P., Lebofsky, L. A., & Tedesco, E. F. 1987, *Nature*, **329**, 522
- Chambers, J. E. 1999, *MNRAS*, **304**, 793
- Cooper, J. F., Christian, E. R., Richardson, J. D., & Wang, C. 2003, *Earth Moon Planets*, **92**, 261
- Cruikshank, D. P., Pilcher, C. B., & Morrison, D. 1976, *Science*, **194**, 835
- Dalle Ore, C. M., et al. 2009, *A&A*, **501**, 349
- de Bergh, C., Delsanti, A., Tozzi, G. P., Dotto, E., Doressoundiram, A., & Barucci, M. A. 2005, *A&A*, **437**, 1115
- Desch, S. J., Cook, J. C., Doggett, T. C., & Porter, S. B. 2009, *Icarus*, **202**, 694
- Doressoundiram, A., Boehnhardt, H., Tegler, S. C., & Trujillo, C. 2008, in *The Solar System Beyond Neptune*, ed. M. A. Barucci, H. Boehnhardt, D. P. Cruikshank, & A. Morbidelli (Tucson, AZ: Univ. Arizona Press), **91**
- Dumas, C., Merlin, F., Barucci, M. A., de Bergh, C., Hainault, O., Guilbert, A., Vernazza, P., & Doressoundiram, A. 2007, *A&A*, **471**, 331
- Emery, J. P., Dalle Ore, C. M., Cruikshank, D. P., Fernández, Y. R., Trilling, D. E., & Stansberry, J. A. 2007, *A&A*, **466**, 395
- Fraser, W. C., & Brown, M. E. 2009, *ApJ*, **695**, L1
- Fulchignoni, M., Belskaya, I., Barucci, M. A., de Sanctis, M. C., & Doressoundiram, A. 2008, in *The Solar System Beyond Neptune*, ed. M. A. Barucci, H. Boehnhardt, D. P. Cruikshank, & A. Morbidelli (Tucson, AZ: Univ. Arizona Press), **181**
- Grundy, W. M., & Schmitt, B. 1998, *J. Geophys. Res.*, **103**, 25809
- Grundy, W. M., Schmitt, B., & Quirico, E. 2002, *Icarus*, **155**, 486
- Hapke, B. 1993, in *Topics in Remote Sensing* (Cambridge: Cambridge Univ. Press)
- Hodapp, K. W., et al. 2003, *PASP*, **115**, 1388

- Houk, N., & Cowley, A. P. (ed.) 1975, University of Michigan Catalogue of Two-dimensional Spectral Types for the HD Stars, Vol. I (Ann Arbor, MI: Univ. Michigan Press), 19
- Jewitt, D. C. 2002, *AJ*, **123**, 1039
- Jewitt, D. C., & Luu, J. 2004, *Nature*, **432**, 731
- Jewitt, D. C., & Luu, J. X. 2001, *AJ*, **122**, 2099
- Malhotra, R. 1993, *Nature*, **365**, 819
- Martini, P., Persson, S. E., Murphy, D. C., Birk, C., Shectman, S. A., Gunnels, S. M., & Koch, E. 2004, *Proc. SPIE*, **5492**, 1653
- McKinnon, W. B., Privalnik, D., Stern, S. A., & Coradini, A. 2008, in *The Solar System Beyond Neptune*, ed. M. A. Barucci, H. Boehnhardt, D. P. Cruikshank, & A. Morbidelli (Tucson, AZ: Univ. Arizona Press), 213
- Merlin, F., Barucci, M. A., de Bergh, C., Fornasier, S., Doressoundiram, A., Perna, D., & Protopapa, S. 2010, *Icarus*, **208**, 945
- Merlin, F., et al. 2009, *AJ*, **137**, 315
- Morbidelli, A., Levison, H. F., & Gomes, R. 2008, in *The Solar System Beyond Neptune*, ed. M. A. Barucci, H. Boehnhardt, D. P. Cruikshank, & A. Morbidelli (Tucson, AZ: Univ. Arizona Press), 275
- Moroz, L., Baratta, G., Strazzulla, G., Starukhina, L., Dotto, E., Barucci, M. A., Arnold, G., & Distefano, E. 2004, *Icarus*, **170**, 214
- Newman, S. F., Buratti, B. J., Brown, R. H., Jaumann, R., Bauer, J., & Momary, T. 2008, *Icarus*, **193**, 397
- Noll, K. S., Luu, J., & Gilmore, D. 2000, *AJ*, **119**, 970
- Olkin, C. B., et al. 2007, *AJ*, **133**, 420
- Pinilla-Alonso, N., Brunetto, R., Licandro, J., Gil-Hutton, R., Roush, T. L., & Strazzulla, G. 2009, *A&A*, **496**, 547
- Porter, S. B., Desch, S. J., & Cook, J. C. 2010, *Icarus*, **208**, 492
- Quirico, E., Doute, S., Schmitt, B., de Bergh, C., Cruikshank, D. P., Owen, T. C., Geballe, T. R., & Roush, T. L. 1999, *Icarus*, **139**, 159
- Rabinowitz, D., & Marsden, B. G. 2010, *Minor Planet Electronic Circulars*, C52
- Ragozzine, D., & Brown, M. E. 2007, *AJ*, **134**, 2160
- Schaller, E. L., & Brown, M. E. 2007a, *ApJ*, **670**, L49
- Schaller, E. L., & Brown, M. E. 2007b, *ApJ*, **659**, L61
- Schaller, E. L., & Brown, M. E. 2008, *ApJ*, **684**, L107
- Sheppard, S. S. 2010, *AJ*, **139**, 1394
- Smith, J. A., et al. 2002, *AJ*, **123**, 2121
- Smith, J. A., et al. 2005, *BAAS*, **37**, 1379
- Snodgrass, C., Carry, B., Dumas, C., & Hainaut, O. 2010, *A&A*, **511**, A72
- Stansberry, J., Grundy, W., Brown, M., Cruikshank, D., Spencer, J., Trilling, D., & Margot, J. 2008, in *The Solar System Beyond Neptune*, ed. M. A. Barucci, H. Boehnhardt, D. P. Cruikshank, & A. Morbidelli (Tucson, AZ: Univ. Arizona Press), 161
- Tiscareno, M. S., & Malhotra, R. 2009, *AJ*, **138**, 827
- Trujillo, C. A., Brown, M. E., Barkume, K. M., Schaller, E. L., & Rabinowitz, D. L. 2007a, *ApJ*, **655**, 1172
- Trujillo, C. A., Brown, M. E., & Rabinowitz, D. L. 2007b, *BAAS*, **38**, 510
- Trujillo, C. A., Brown, M. E., Rabinowitz, D. L., & Geballe, T. R. 2005, *ApJ*, **627**, 1057
- Wenger, M., et al. 2000, *A&AS*, **143**, 9